

Review Article

Synchrotron-Radiation X-Ray Investigation of Li^+/Na^+ Intercalation into Prussian Blue Analogues

Yutaka Moritomo,^{1,2} Masamitsu Takachi,¹ Yutaro Kurihara,¹ and Tomoyuki Matsuda¹

¹ Graduate School of Pure and Applied Science, University of Tsukuba, Tsukuba 305-8571, Japan

² Tsukuba Research Center for Interdisciplinary Materials Science (TIMS), University of Tsukuba, Tsukuba 305-8571, Japan

Correspondence should be addressed to Yutaka Moritomo; moritomo@sakura.cc.tsukuba.ac.jp

Received 19 June 2013; Accepted 26 August 2013

Academic Editor: Gerhard Schumacher

Copyright © 2013 Yutaka Moritomo et al. This is an open access article distributed under the Creative Commons Attribution License, which permits unrestricted use, distribution, and reproduction in any medium, provided the original work is properly cited.

Prussian blue analogies (PBAs) are promising cathode materials for lithium ion (LIB) and sodium ion (SIB) secondary batteries, reflecting their covalent and nanoporous host structure. With use of synchrotron-radiation (SR) X-ray source, we investigated the structural and electronic responses of the host framework of PBAs against Li^+ and Na^+ intercalation by means of the X-ray powder diffraction (XRD) and X-ray absorption spectroscopy (XAS). The structural investigation reveals a robust nature of the host framework against Li^+ and Na^+ intercalation, which is advantageous for the stability and lifetime of the batteries. The spectroscopic investigation identifies the redox processes in respective plateaus in the discharge curves. We further compare these characteristics with those of the conventional cathode materials, such as, LiCoO_2 , LiFePO_4 , and LiMn_2O_4 .

1. Introduction

1.1. Brief History of Lithium Ion Secondary Battery. Lithium is the most base and lightest metal element. Therefore, “lithium metal secondary battery,” whose anode is Li metal, is expected to exhibit the highest energy density [= (voltage versus Li) (capacity/mass)]. The development of “lithium metal secondary battery” started from the 70s. In 1986, a Canadian company commercialized a Li/MoS_2 cell, which exhibits an average working voltage of 3 V. The production, however, stopped due to firings and explosions of the cell. After that, the researchers tried to explore the safer anode materials and finally found that graphite (C_6) exhibits the Li^+ intercalation/deintercalation between the C_6 sheets. In addition, LiCoO_2 with layered rocksalt structure is found to exhibit the Li^+ intercalation/deintercalation between the CoO_2 layers. In 1991, Sony cooperation firstly commercialized a $\text{C}_6/\text{LiCoO}_2$ cell, which exhibits an average operating voltage of 3.9 V. The cell is called “lithium ion secondary battery” (LIB), because the cell does not use dangerous Li metal. Today, the high volume and gravimetric energy density of LIBs have realized mobile electrics, such as smart phone and mobile computer. However, cost, safety, stored energy density,

charge/discharge rate, and service life are still issues that force the development of LIBs for the potential mass market of electric vehicle [1, 2].

Here, let us survey electrochemical and structural/electronic properties the the conventionally used cathode materials for LIBs. LiCoO_2 with layered rock-salt structure is the most prototypical cathode material for LIBs, which exhibits an average working voltage of 3.9 V against Li. The material consists of covalently bonded CoO_2 layers and Li^+ , which is accommodated between the layers. The ideal capacity, $\text{LiCoO}_2 \rightarrow \text{CoO}_2 + \text{Li}$, is 274 mAh/g, which is realized with the charge voltage of 4.7 V. The Li^+ deintercalation, however, causes successive structural phase transitions due to the Li^+ ordering and eventually produces CoO_2 with CdI_2 structure. So, in the actual use of the cell, the cutoff voltage is set to be below 4 V. The $\text{C}_6/\text{LiCoO}_2$ cell exhibits a practical capacity of 150 mAh/g. LiFePO_4 with ordered-olivine structure exhibits an average working voltage of 3.5 V against Li. The material consists of one-dimensional (1D) framework made by covalently connected PO_4 tetrahedron and FeO_6 octahedron and Li^+ , which is accommodated in the tube-type interstitial sites. The ideal capacity, $\text{LiFePO}_4 \rightarrow \text{FePO}_4 + \text{Li}$, is 170 mAh/g. The Li deintercalation, however, causes phase separation into

LiFePO₄ and FePO₄. In addition, LiFePO₄ is an insulator with low electron conductivity ($\sigma < 10^{-8} \Omega \text{ cm}$), which is disadvantageous for the high charge/discharge rate. Fortunately, a carbon-coating procedure mysteriously improves the rate properties of LiFePO₄. LiMn₂O₄ with spinel structure exhibits an average working voltage of 4 V against Li. In this material, Li⁺ does not occupy the interstitial sites, but three-dimensionally connects the MnO₆ octahedra. The ideal capacity, LiMn₂O₄ → Mn₂O₄ + Li, is 285 mAh/g. γ -MnO₂, however, is produced at low Li concentration region. The C₆/LiMn₂O₄* cell exhibits practical capacity of 140 mAh/g.

1.2. Sodium Ion Secondary Battery. Sodium ion secondary battery (SIB) is a promising candidate for the next-generation battery beyond the lithium ion secondary battery (LIB) with safe, environmentally friendly, and low-cost characteristics. The SIB device stores the electric energy utilizing intercalation/deintercalation process of abundant Na⁺ (Clark number = 2.63), instead of rare Li⁺ (0.006), within the cathode and anode materials. In this sense, the SIB is suitable for a large-scale battery for stable use of the solar and wind energies. Among a variety of cathode materials for SIB [3, 4], Na_xMO₂ (*M* is transition metal element) with layered structure exhibits promising electrochemical properties as well as rich structural properties. In particular, the replacement of Na⁺ for Li⁺ significantly expands the choice of the transition metals. For example, NaCrO₂ [5] with α -NaFeO₂ structure exhibits a capacity of 120 mAh/g and an average operating voltage of 3.0 V with a good cyclability in SIB, while isostructural LiCrO₂ exhibits poor capacity and cyclability in LIB. Na_{0.6}MnO₂ [6] with P2-type structure exhibits a capacity of 140 mAh/g and an average operating voltage of 2.5 V. Recently, a coin-type full SIB cell with hard carbon/NaNi_{0.5}Mn_{0.5}O₂ configuration is demonstrated to exhibit a high capacity more than 200 mAh/g (anode basis) and an average operating voltage of 3 V with a good cyclability [7]. This demonstration opens the view to commercial utilization of SIBs and hence significantly stimulates investigation and exploration of cathode materials for SIBs.

1.3. Overview of Prussian Blue Analogues. Prussian blue analogue (PBA), A_xM[Fe(CN)₆]_yzH₂O (*A* and *M* are alkali metal and transition metal, resp.), is the oldest complex compound that the human being has synthesized. The PBAs consist of a three-dimensional (3D) cyano-bridged transition metal framework (*M*[Fe(CN)₆]_y) and guests (*A*⁺ and H₂O) accommodated at the cubic nanopores, as schematically shown in Figure 1. Parts of the waters (ligand water) locate at the [Fe(CN)₆] vacancies and coordinate to *M*. The residual waters (zeolite water) and alkali cations (*A*⁺) locate in the nanopores of the host framework. Most of the PBAs exhibit face-centered cubic structure (Fm $\bar{3}$ m; *Z* = 4) [8]. The PBAs are attracting current interest of material scientists, because they exhibit useful functionalities, such as LIB properties [9–12], SIB properties [13–15], and electrochromism [16, 17].

Interestingly, the size of the nanopores can be controlled by the substitution of *M*: the lattice constant (*a*) linearly increases with the ionic size (*r*_M) of *M* as a (nm) = 0.891 +

$2r_M$ (nm) in (Cs, Rb)_xM^{II}[Fe^{III}(CN)₆]_y (*M* = Co, Fe, Ni, Cu, Zn, Mn, and Cd) [8]. Historically, the alkali cation intercalation was interpreted in terms of the hydrated radius (*r*_H) [22–24], rather than the ionic radius (*r*_A) of bare alkali cation. Actually, Tieke's group [23, 24] reported that the self-assembled films of PBAs are permeable to smaller hydrated ions such as Cs⁺ (*r*_H = 0.119 nm) and K⁺ (*r*_H = 0.125 nm), whereas they block bigger hydrated ions such as Na⁺ (*r*_H = 0.184 nm). These films, however, consist of microcrystals with considerable [Fe(CN)₆] vacancies (*y* ~ 0.67). On the other hand, Moritomo et al. [25] electrochemically synthesized a thin film of crystalline Na_{0.76}Co[Fe(CN)₆]_{0.90}2.9H₂O (*y* = 0.9) with fewer vacancies. They observed that the intercalation of Na⁺ (*r*_A = 0.118 nm) is much faster than those of K⁺ (*r*_A = 0.151 nm) and Rb⁺ (*r*_A = 0.161 nm). This observation suggests that the intrinsic alkali cation intercalation should be interpreted in terms of *r*_A: Li⁺ (*r*_A = 0.092 nm), Na⁺ (0.118 nm), K⁺ (0.151 nm), Rb⁺ (0.161 nm), and Cs⁺ (0.174 nm). They further demonstrated that the intercalation behavior is qualitatively explained by the cation potentials based on the *ab initio* calculation.

1.4. Prussian Blue Analogues as Cathode Materials. The PBAs are promising cathode materials for LIBs and SIBs. Imanishi et al. [9, 10] reported Li⁺ intercalation behaviors in *M*[Fe(CN)₆]_y (*M* = V, Mn, Fe, Ni, and Cu), even though their cyclability is far from satisfactory. The cyclability is fairly improved in K_{0.10}Mn^{II}[Fe^{III}(CN)₆]_{0.70}4.2H₂O and Rb_{0.61}Mn^{II}[Fe^{III}(CN)₆]_{0.87}2.2H₂O [11]. Matsuda et al. [12] synthesized a manganese hexacyanoferrate thin film, Li_{1.32}Mn^{II}[Fe^{II}(CN)₆]_{0.83}3.5H₂O, with high Li concentration (*x* = 1.32). They reported that the thin-film electrode exhibits a high capacity of 128 mAh/g and an average operating voltage of 3.6 V against Li with a good cyclability. Recently, Goodenough's group [13] reported Na⁺ intercalation behaviors in a *K-M-Fe(CN)₆* system (*M* = Mn, Fe, Co, Ni, Cu, and Zn). However, their coulomb efficiency (=60% for *M* = Fe), that is, the ratio of discharge capacity and charge capacity, is very low. The low efficiency suggests an irreversible redox process in addition to the reversible Na⁺ intercalation/deintercalation process. Matsuda et al. [14] investigated electrochemical properties of film electrode of Na_{1.32}Mn^{II}[Fe^{II}(CN)₆]_{0.83}3.5H₂O and reported a high capacity of 109 mAh/g and an average operating voltage of 3.4 V against Na with a good cyclability. In addition, Takachi et al. [15] reported that Na_{1.60}Co^{II}[Fe^{II}(CN)₆]_{0.90}2.9H₂O film electrode exhibits a high capacity of 135 mAh/g and an average operating voltage of 3.6 V against Na with a good cyclability.

In this paper, with use of synchrotron-radiation (SR) X-ray source, we investigated the structural and electronic responses of the host framework of PBA against Li⁺ and Na⁺ intercalation by means of the X-ray powder diffraction (XRD) and X-ray absorption spectroscopy (XAS). The structural investigation reveals a robust nature of the host framework against Li⁺ and Na⁺ intercalation, which is advantageous for the stability and lifetime of the batteries. The spectroscopic investigation identifies the redox processes in respective plateaus in the discharge curves. We further compare these

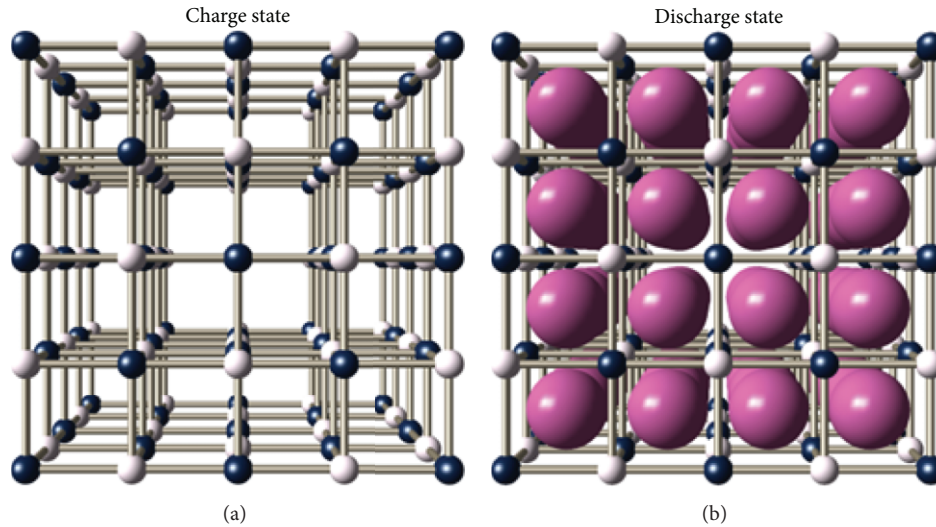


FIGURE 1: Schematic structures of PBA, $A_xM[\text{Fe}(\text{CN})_6]_y \cdot z\text{H}_2\text{O}$ (A and M are alkali metal and transition metal, resp.) in charge (a) and discharge (b) states. Transition metal and iron (small spheres) are alternatively bridged by the cyano groups (sticks). Big spheres represent the guest alkali cations. Water molecules are omitted for simplicity.

TABLE 1: Electrolyte compositions in the electrochemical deposition of the respective PBA films. NMF83, NMF87, NMF93, NCF90, NCF71, NNF68, and NCdF96 represent $\text{Na}_{1.24}\text{Mn}[\text{Fe}(\text{CN})_6]_{0.81} \cdot 3.0\text{H}_2\text{O}$, $\text{Na}_{1.48}\text{Mn}[\text{Fe}(\text{CN})_6]_{0.87} \cdot 2.5\text{H}_2\text{O}$, $\text{Na}_{1.72}\text{Mn}[\text{Fe}(\text{CN})_6]_{0.93} \cdot 2.3\text{H}_2\text{O}$, $\text{Na}_{1.60}\text{Co}[\text{Fe}(\text{CN})_6]_{0.90} \cdot 2.9\text{H}_2\text{O}$, $\text{Na}_{0.84}\text{Co}[\text{Fe}(\text{CN})_6]_{0.71} \cdot 3.8\text{H}_2\text{O}$, $\text{Na}_{0.72}\text{Ni}[\text{Fe}(\text{CN})_6]_{0.68} \cdot 5.1\text{H}_2\text{O}$, and $\text{Na}_{1.84}\text{Cd}[\text{Fe}(\text{CN})_6]_{0.96} \cdot 4.8\text{H}_2\text{O}$, respectively.

Film	Electrolytes		
NMF83	1.0 mmol/L $\text{K}_3[\text{Fe}(\text{CN})_6]$	1.5 mmol MnCl_2	1 mol/L NaCl
NMF87	1.0 mmol/L $\text{K}_3[\text{Fe}(\text{CN})_6]$	1.5 mmol MnCl_2	3 mol/L NaCl
NMF93	1.0 mmol/L $\text{K}_3[\text{Fe}(\text{CN})_6]$	1.5 mmol MnCl_2	5 mol/L NaCl
NCF90	0.8 mmol/L $\text{K}_3[\text{Fe}(\text{CN})_6]$	0.5 mmol $\text{Co}(\text{NO}_3)_2$	5 mol/L NaNO_3
NCF71	0.5 mmol/L $\text{K}_3[\text{Fe}(\text{CN})_6]$	1.25 mmol $\text{Co}(\text{NO}_3)_2$	1 mol/L NaNO_3
NNF68	0.5 mmol/L $\text{K}_3[\text{Fe}(\text{CN})_6]$	0.5 mmol $\text{Ni}(\text{NO}_3)_2$	1 mol/L NaNO_3
NCdF96	1.0 mmol/L $\text{K}_3[\text{Fe}(\text{CN})_6]$	1.5 mmol MnCl_2	1 mol/L NaCl

characteristics with those of the conventional cathode materials, such as LiCoO_2 , LiFePO_4 , and LiMn_2O_4 .

2. Experimental Method

2.1. Preparation of Films. Thin films of $\text{Na}_{1.32}\text{Mn}[\text{Fe}(\text{CN})_6]_{0.83} \cdot 3.5\text{H}_2\text{O}$ (denoted as NMF83), $\text{Na}_{1.48}\text{Mn}[\text{Fe}(\text{CN})_6]_{0.87} \cdot 2.5\text{H}_2\text{O}$ (NMF87), $\text{Na}_{1.72}\text{Mn}[\text{Fe}(\text{CN})_6]_{0.93} \cdot 2.3\text{H}_2\text{O}$ (NMF93), $\text{Na}_{1.60}\text{Co}[\text{Fe}(\text{CN})_6]_{0.90} \cdot 2.9\text{H}_2\text{O}$ (NCF90), $\text{Na}_{0.84}\text{Co}[\text{Fe}(\text{CN})_6]_{0.71} \cdot 3.8\text{H}_2\text{O}$ (NCF71), $\text{Na}_{0.72}\text{Ni}[\text{Fe}(\text{CN})_6]_{0.68} \cdot 5.1\text{H}_2\text{O}$ (NNF68), and $\text{Na}_{1.84}\text{Cd}[\text{Fe}(\text{CN})_6]_{0.96} \cdot 4.8\text{H}_2\text{O}$ (NCdF96) were electrochemically synthesized on an indium tin oxide (ITO) transparent electrode under potentiostatic conditions at -0.50 V versus a standard Ag/AgCl electrode in aqueous solutions. The electrolyte compositions of the aqueous solutions are summarized in Table 1. Typical thickness of the films is ca. $1 \mu\text{m}$, which was measured with a profilometer (Dektak3030). The mass of each film was measured with a conventional electronic weighing machine after the film was carefully removed from the ITO glass with a microspatula.

The experimental error of the mass is ca. 10%. Chemical compositions of the films were determined by the inductively coupled plasma (ICP) method and CHN organic elementary analysis (Perkin-Elmer 2400 CHN Elemental Analyzer). NMF83, NCF90, NCF71, NNF68, and NCdF96 exhibit face-centered cubic structure. The lattice constants (a) are 10.544(2) Å for NMF83, 10.404(2) Å for NCF90, 10.296(2) Å for NCF71, 10.200(3) Å for NNF68, and 10.7001(4) Å for NCdF96. On the other hand, NMF87 and NMF93 exhibit trigonal distortion, reflecting the guest-host interaction [26].

The Li compounds were synthesized by electrochemical substitution of Li^+ for Na^+ within a beaker-type cell against Li. The electrolyte was ethylene carbonate (EC)/diethyl carbonate (DEC) solution containing 1 mol/L LiClO_4 . The charge/discharge current was ca. $5 \mu\text{A}/\text{cm}^2$, and the cutoff voltage was from 2.0 to 4.2 V. The active area of the film was about 2.0 cm^2 . We obtained Li-substituted films: $\text{Li}_{1.32}\text{Mn}[\text{Fe}(\text{CN})_6]_{0.83} \cdot 3.5\text{H}_2\text{O}$ (LMF83), $\text{Li}_{1.48}\text{Mn}[\text{Fe}(\text{CN})_6]_{0.87} \cdot 2.5\text{H}_2\text{O}$ (LMF87), $\text{Li}_{1.72}\text{Mn}[\text{Fe}(\text{CN})_6]_{0.93} \cdot 2.3\text{H}_2\text{O}$ (LMF93), $\text{Li}_{1.60}\text{Co}[\text{Fe}(\text{CN})_6]_{0.90} \cdot 2.9\text{H}_2\text{O}$ (LCF90), $\text{Li}_{0.71}\text{Na}_{0.13}\text{Co}[\text{Fe}(\text{CN})_6]_{0.71} \cdot 3.8\text{H}_2\text{O}$ (LCF71), $\text{Li}_{0.68}\text{Na}_{0.04}\text{Ni}[\text{Fe}(\text{CN})_6]_{0.68}$

TABLE 2: Abbreviation, compositions, and Li/Na concentration (x) in discharge and charge states.

Film	Composition	Discharge state	Charge state
LMF83	$\text{Li}_x\text{Mn}[\text{Fe}(\text{CN})_6]_{0.83}3.5\text{H}_2\text{O}$	$x = 1.32$	$x = 0.00$
LMF87	$\text{Li}_x\text{Mn}[\text{Fe}(\text{CN})_6]_{0.87}2.5\text{H}_2\text{O}$	$x = 1.48$	$x = 0.00$
LMF93	$\text{Li}_x\text{Mn}[\text{Fe}(\text{CN})_6]_{0.93}2.3\text{H}_2\text{O}$	$x = 1.72$	$x = 0.00$
LCF90	$\text{Li}_x\text{Co}[\text{Fe}(\text{CN})_6]_{0.90}2.9\text{H}_2\text{O}$	$x = 1.60$	$x = 0.00$
LCF71	$\text{Li}_x\text{Na}_{0.13}\text{Co}[\text{Fe}(\text{CN})_6]_{0.71}3.8\text{H}_2\text{O}$	$x = 0.71$	$x = 0.00$
LNF68	$\text{Li}_x\text{Na}_{0.04}\text{Ni}[\text{Fe}(\text{CN})_6]_{0.68}5.1\text{H}_2\text{O}$	$x = 0.68$	$x = 0.00$
LCdF96	$\text{Li}_x\text{Na}_{0.88}\text{Cd}[\text{Fe}(\text{CN})_6]_{0.96}4.8\text{H}_2\text{O}$	$x = 0.96$	$x = 0.00$
NMF83	$\text{Na}_x\text{Mn}[\text{Fe}(\text{CN})_6]_{0.83}3.5\text{H}_2\text{O}$	$x = 1.32$	$x = 0.00$
NCF90	$\text{Na}_x\text{Co}[\text{Fe}(\text{CN})_6]_{0.90}2.9\text{H}_2\text{O}$	$x = 1.60$	$x = 0.00$

5.1H₂O (LNF68), and Li_{0.96} Na_{0.88}Cd[Fe(CN)₆]_{0.96}4.8H₂O (LCdF96).

2.2. Electrochemical Measurement. The discharge/charge measurement was performed in a beaker-type cell. For the Li⁺ intercalation/deintercalation process, the PBA films and the Li metal were used as the cathode and anode, respectively. The active area of the film was about 2.0 cm². The electrolyte was EC/DEC solution containing 1 mol/L LiClO₄. The cutoff voltage was from 2.0 to 4.2 V. For the Na⁺ intercalation/deintercalation process, the PBA films and the Na metal were used as the cathode and anode, respectively. The active area of the film was about 2.0 cm². The electrolyte was propylene carbonate (PC) solution containing 1 mol/L NaClO₄. The cut-off voltage was from 2.0 to 4.2 V.

For the *ex situ* XRD and XAS experiments, the Li/Na concentration (x) of the PBA film was controlled by the charge/discharge process in a beaker-type cell. The discharge capacities of the respective PBA films are close to the ideal values. Therefore, the magnitude of Li concentration (x) is determined by the current with assuming nominal chemical compositions in the charge and discharge states. Similarly, the magnitude of Na concentration (x) is determined by the current with assuming nominal chemical compositions in the charge and discharge states. In Table 2, abbreviation, chemical compositions, and Li/Na concentration (x) in the discharge and charge states are summarized.

2.3. X-Ray Powder Diffraction Measurement. The *ex situ* XRD measurements were performed at the BL02B2 beamline [27] of SPring-8 and 8A beamline of the Photon Factory, KEK. The films were carefully removed from the ITO glass with a microspatula in air atmosphere. The fine powder samples were filled and sealed in a 0.3 mm ϕ glass capillary. In the entire x -region, the films were stable in air for at least 1h. The capillary was placed on a Debye-Scherrer camera. The powder diffraction patterns were detected with an imaging plate (IP) at 300 K. The exposure time was 5 min. The wavelength of the X-ray was calibrated by the lattice constant of standard CeO₂ powders ($a = 5.41111$ Å). Thus obtained powder diffraction patterns are analyzed by the Rietveld method (Rietan-FP program [28]).

2.4. X-Ray Absorption Measurement. The *ex situ* XAS measurements were performed at beamline 7C of the Photon Factory, KEK. The XAS spectra were measured in a fluorescent yield mode with a Lytle detector at 300 K. The X-ray was monochromatized with a Si(111) double-crystal monochromator. At the XAS measurement for respective elements, for example, Mn, Fe, Co, and Ni, the monochromator was calibrated by the K-edge of the respective metal foils. The PBA films were sealed in plastic to avoid air exposure. The background subtraction, normalization, and component decomposition were performed with ATHENA program [29]. The valence states of the constituent transition metals, that is, Mn, Fe, Co, Ni, and Cd, are determined by the XAS spectra around the Mn K-, Fe K-, Co K-, Ni K-, and Cd L₁-edges.

In the X-ray fluorescence measurements, we should be careful to the two types of the self-absorption effects. One is the absorption of the fluoresced X-rays and the other one is that of the incident X-ray. In Table 3, the penetration depths (λ) for ideal Na₂Mn[Fe(CN)₆] and Na₂Co[Fe(CN)₆] are listed at the fluorescence and absorption energies of the Mn, Fe, and Co K-edges. The λ values are much bigger than the thickness (~ 1 μm) of the film. In this condition, the absorbed photon ($= 1 - e^{-\alpha d}$; α is the absorption coefficient) by the film is proportional to α .

3. Li⁺ Intercalation

3.1. Manganese PBA. Figure 2 shows the open-current-voltage (OCV) discharge curve of NMF83 film against Li measured at 0.05 C. The discharge curve shows two plateaus at 3.8 (plateau I) and 3.5 V (plateau II). The observed capacity (=115 mAh/g) is comparable to the ideal value (=110 mAh/g).

Figure 3 shows the XRD patterns of powered LMF83 against Li concentration (x). All the reflections can be indexed with the face-centered cubic setting, as shown in parentheses. No structural phase transition nor phase separation is observed in the entire x -region. The lattice constants (a) are refined by Rietveld analysis with the face-centered cubic (Fm $\bar{3}$ m; $Z = 4$) model.

Figure 4(a) shows the XAS spectra of LMF83 films around the Fe K-edge against x . The peak energy at $x = 1.32$ coincides with that of low-spin (LS) Fe²⁺ [30]. The blue-shift with decrease in x indicates partial formation of LS Fe³⁺. The peak

TABLE 3: Penetration depths (λ) for ideal $\text{Na}_2\text{Mn}[\text{Fe}(\text{CN})_6]$ and $\text{Na}_2\text{Co}[\text{Fe}(\text{CN})_6]$ at the fluorescence and absorption energies of the Mn, Fe, and Co K-edges.

Photon energy		λ for $\text{Na}_2\text{Mn}[\text{Fe}(\text{CN})_6]$	λ for $\text{Na}_2\text{Co}[\text{Fe}(\text{CN})_6]$
5900 eV	Mn fluorescence	104 μm	96 μm
6405 eV	Fe fluorescence	132 μm	121 μm
6930 eV	Co fluorescence	55 μm	151 μm
6539 eV	Mn K-edge	139 μm	128 μm
7112 eV	Fe K-edge	59 μm	162 μm
7709 eV	Co K-edge	41 μm	38 μm

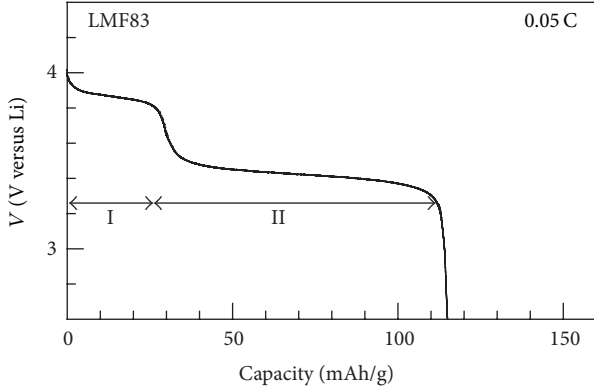


FIGURE 2: OCV discharge curves of LMF83 film against Li measured at 0.05 C. For convenience of explanation, we define plateaus I and II (cited from [18]).

energy at $x = 0.00$ coincides with that of LS Fe^{3+} [30]. In other words, all the Fe sites are oxidized in the charge state. The electronic configuration at $x = 0.00$ becomes $\text{Mn}^{2.49+} - \text{Fe}^{3+}$ if we assume the charge neutrality: $\text{Li}_{1.32}\text{Mn}^{\text{II}}[\text{Fe}^{\text{II}}(\text{CN})_6]_{0.83} \rightarrow 1.6\text{Li}^+ + \text{Mn}_{0.51}^{\text{II}}\text{Mn}_{0.49}^{\text{III}}[\text{Fe}^{\text{III}}(\text{CN})_6]_{0.83}$. The average Fe valence (V_{Fe}) is determined by the peak energy (E) as $V_{\text{Fe}} = -6569.0 + 0.92204E$. Figure 4(b) shows the XAS spectra of LMF83 films around the Mn K-edge against x . In the low x -region, a shoulder structure appears around 6553 eV. The absorption is ascribed to Mn^{3+} state. The Mn valence (V_{Mn}) is estimated from the relative intensity (I) at 6553 eV as $V_{\text{Mn}} = 2 + 0.49 * [I(x) - I(0.00)] / [I(1.32) - I(0.00)]$.

Thus obtained lattice constant (a), Mn valence, and the Co valence are plotted in Figure 5. In the plateau I ($0.0 < x < 0.4$), the Mn valence decreases while the Fe valence remains trivalent. In the plateau II ($0.4x < 1.32$), the Fe valence decreases while Mn valence remains divalent. These observations clearly indicate that the plateaus I and II are ascribed to the reduction processes of Mn^{3+} and Fe^{3+} , respectively. Surprisingly, LMF83 remains single cubic phase without structural phase transition nor phase separation in the entire x -region. In the plateau I, the lattice constant steeply increases from 10.40 Å at $x = 0.00$ to ~ 10.58 Å at $x \sim 0.4$. The expansion is ascribed to the bigger ionic radius ($=0.83$ Å) of high-spin (HS) Mn^{2+} than that ($=0.65$ Å) of HS Mn^{3+} . On the other hand, the lattice constant slightly decreases with increasing in x in the plateau II. The decrease

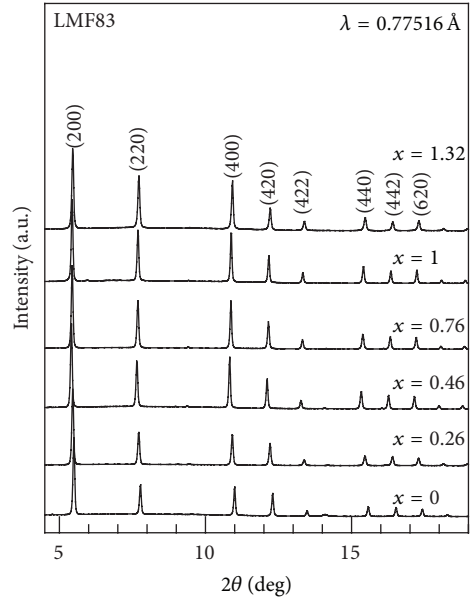


FIGURE 3: XRD pattern of powered LMF83 against Li concentration (x). Values in parentheses represent indexes in the face-centered cubic setting (cited from [19]).

is probably due to the smaller size of $[\text{Fe}^{\text{II}}(\text{CN})_6]^{4-}$ than that of $[\text{Fe}^{\text{III}}(\text{CN})_6]^{3-}$. Actually, the $\text{Fe}^{\text{II}}-\text{N}$ distance ($=3.00 - 3.01$ Å) is shorter than the $\text{Fe}^{\text{III}}-\text{N}$ distance ($=3.10$ Å) in $\text{RbMn}[\text{Fe}(\text{CN})_6]$ [31].

In manganese PBA, $\text{Li}_x\text{Mn}[\text{Fe}(\text{CN})_6]_y$, both the transition metals, that is, Mn and Fe, take part in the redox process. Then, the capacity is expected to increase with sum of the transition metal concentration ($1 + y$). Strictly speaking, however, the capacity increases with the initial Li concentration (x_0), because $x_0 (=4y - 2)$ is lower than $1 + y$ in the entire y -region ($0 < y < 1$). Figure 6 shows the OCV discharge curves of manganese PBA films against Li: LMF83 ($y = 0.83$), LMF87 ($y = 0.87$), and LMF93 ($y = 0.93$). As expected, the capacity increases with y : 115 mAh/g for LMF83, 130 mAh/g for LMF87, and 143 mAh/g for LMF93. These values are comparable to the ideal values, 110 mAh/g for LMF83, 134 mAh/g for LMF87, and 153 mAh/g for LMF93. Similarly to the case of the LMF83 film, LMF87 and LMF93 films exhibit two plateaus at 3.8 (plateau I) and 3.5 V (plateau II). Then, the plateaus I and II are reasonably ascribed to the reduction process of Mn^{3+} and Fe^{3+} , respectively. This

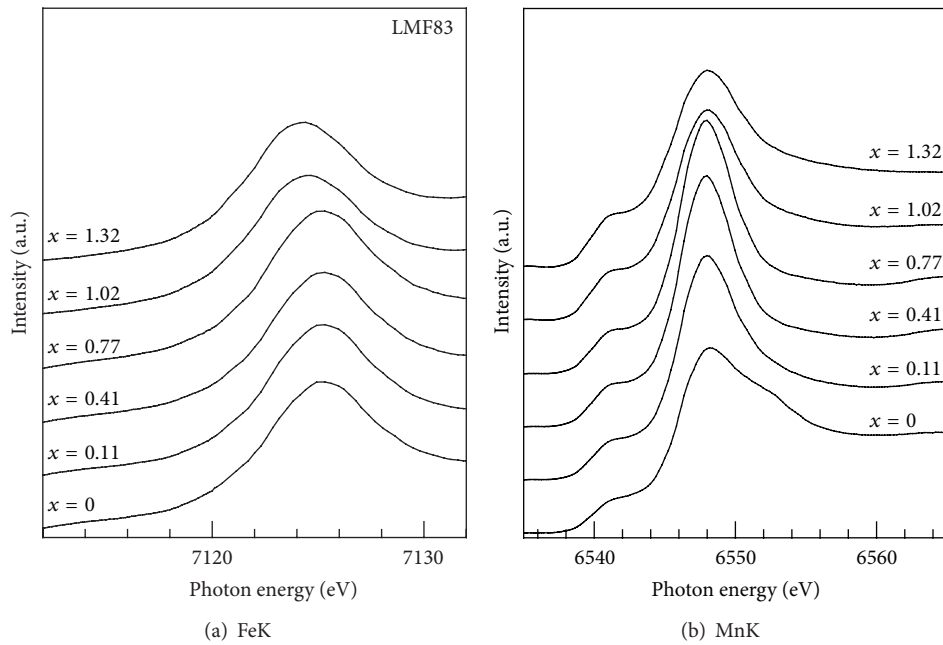


FIGURE 4: XAS spectra of LMF83 films against x around the (a) Fe K- and (b) Mn K-edges (cited from [19]).

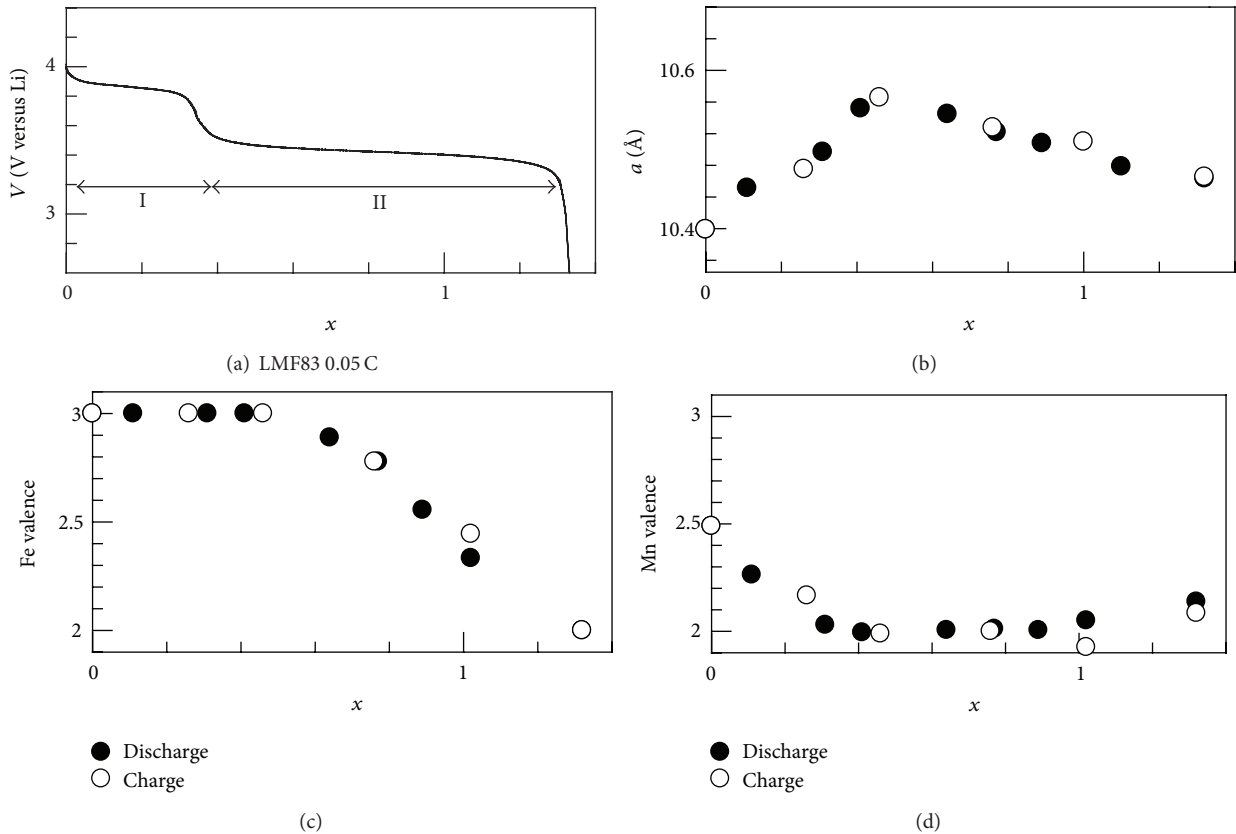


FIGURE 5: (a) Discharge curve, (b) lattice constant a , (c) Fe valence, and (d) Mn valence of NMF83 against x . Open (filled) marks in (b), (c), and (d) mean that the data are obtained in the charge (discharge) run (cited from [19]).

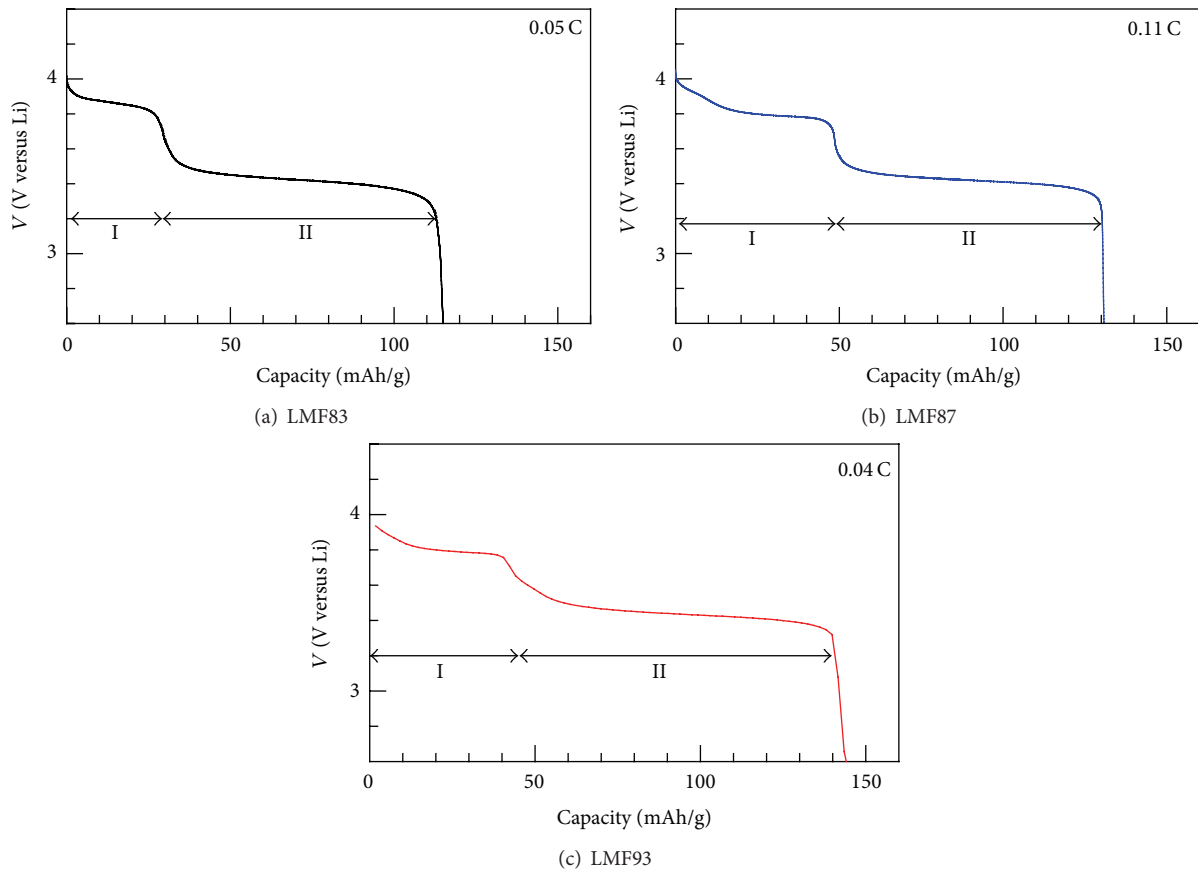


FIGURE 6: OCV discharge curves of (a) LMF83, (b) LMF87, and (c) LMF93 films against Li. For convenience of explanation, we define plateaus I and II (cited from [18]).

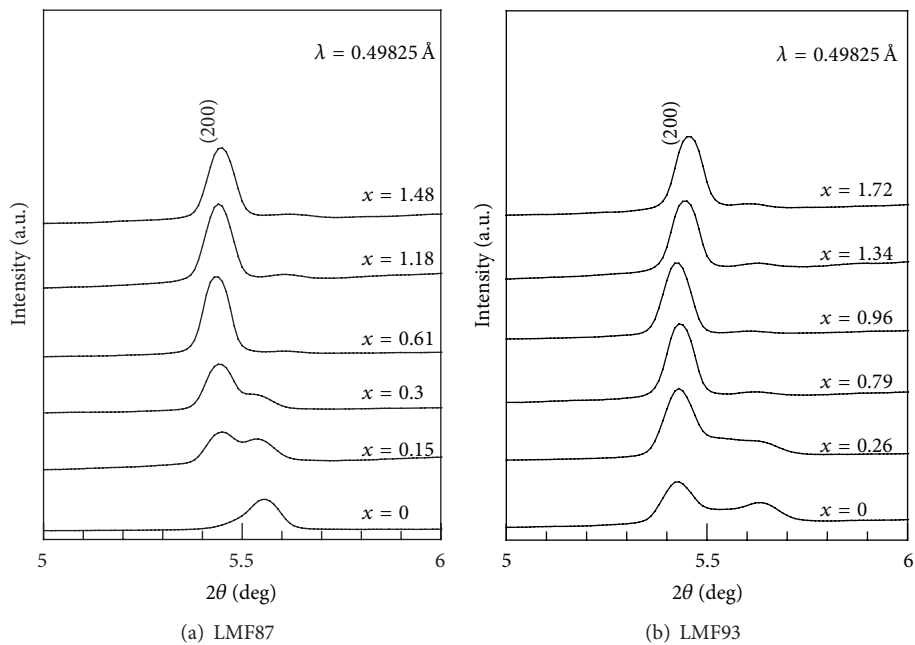


FIGURE 7: Magnified XRD patterns of (a) LMF87 and (b) LMF93 against x. Values in the parentheses represent indexes in the face-centered-cubic setting (cited from [18]).

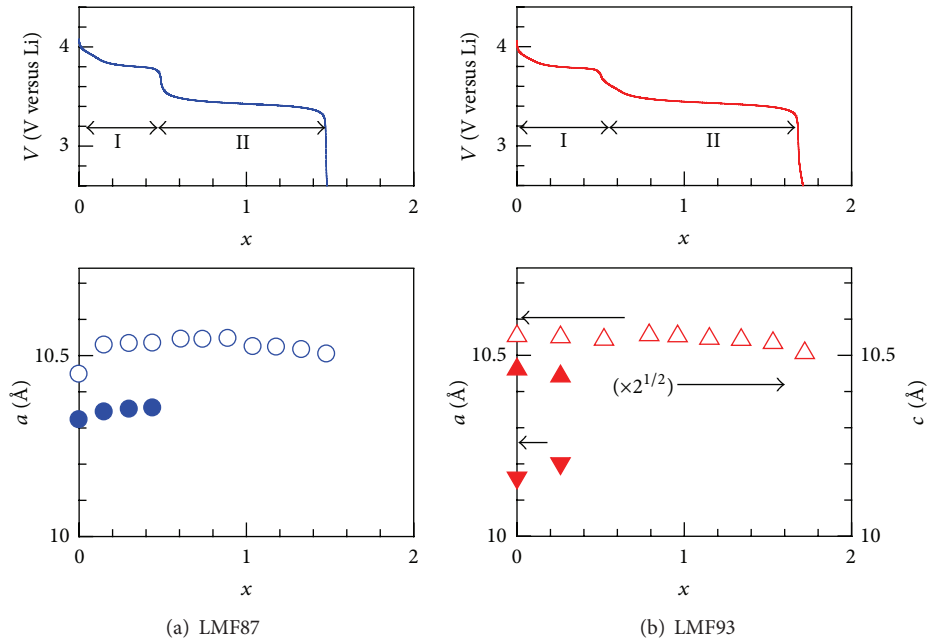


FIGURE 8: Discharge curve and lattice constant (a) of (a) LMF87 and (b) LMF93 against x . Filled marks represent the second tetragonal phase (cited from [18]).

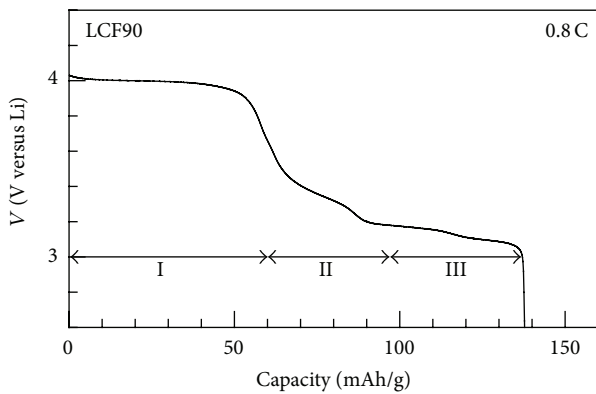


FIGURE 9: OCV discharge curves of LCF90 film against Li measured at 0.8 C. For convenience of explanation, we define plateaus I, II, and III (cited from [20]).

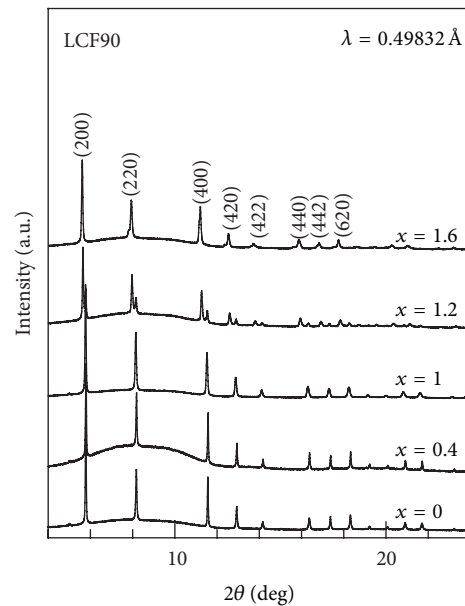


FIGURE 10: XRD pattern of powered LCF90 against x . Values in parentheses represent indexes in the face-centered cubic setting (cited from [20]).

assignments are confirmed by the infrared absorption (IR) spectroscopy around the CN stretching mode region [18].

Figure 7 shows the XRD patterns of (a) LMF83 and (b) LMF93 against x . Similarly to the case of LMF83, the XRD patterns of LMF87 and LMF93 in the high x -region can be indexed with the face-centered cubic setting. In the low x -region, however, two phase features are observed. The extra reflections are indexed with the face-centered cubic ($Fm\bar{3}m$; $Z = 4$) setting in LMF87, while they are indexed with the tetragonal ($I4m2$; $Z = 2$) setting in LMF93. The lattice constants are refined by the Rietveld analysis with the single- and two-phase models.

Figures 8(a) and 8(b) show the lattice constants against x . In plateau II, where the Fe sites are selectively reduced with

x , the lattice constant remains nearly constant. In plateau I, where the Mn sites are selectively reduced with x , two-phase features are observed. In (a) LMF87, a phase separation into two cubic phases takes place below $x = 0.44$. The volume fraction of the second phase increases as x decreases. In (b) LMF93, a phase separation into cubic and tetragonal phases takes place below $x = 0.26$. The volume fraction of the second phase increases as x decreases.

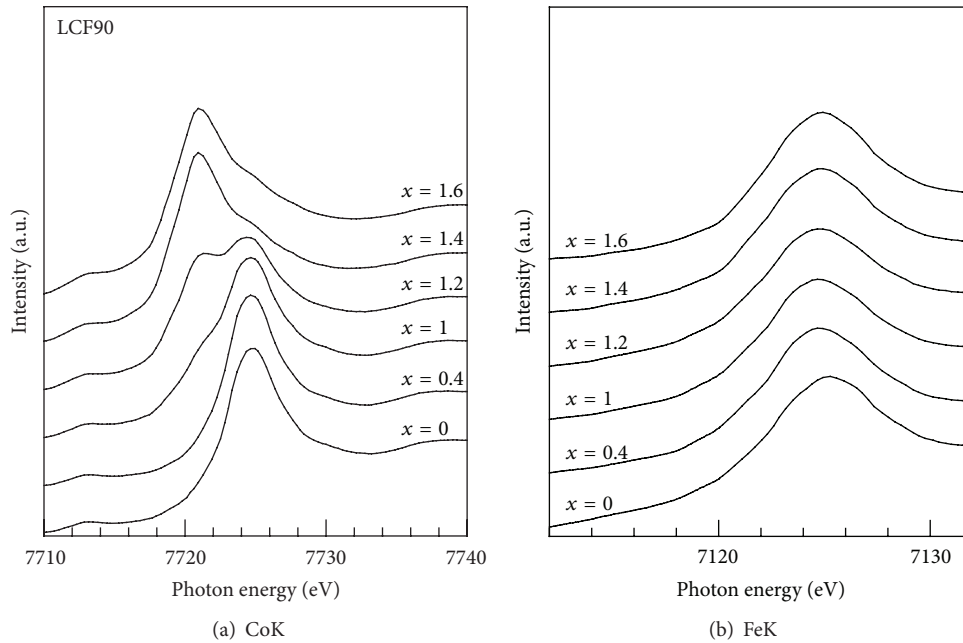


FIGURE 11: XAS spectra of LCF90 films against x around the (a) Co K- and (b) Fe K-edges (cited from [20]).

The most probable origin of the phase separation in the Li intercalation system is the spontaneous phase separation into the Li-rich and Li-poor regions. Actually, Li_xFePO_4 exhibits a phase separation into LiFePO_4 and FePO_4 in most of the x -region [32]. In the present manganese PBA, the coexistence of bigger Mn^{2+} and smaller Mn^{3+} may cause the local strain in the low x -region. In this situation, the system tends to exhibit a spontaneous phase separation into the Li-rich (Mn^{2+} -rich) and Li-poor (Mn^{3+} -rich) regions to release the local strain. In this scenario, the second phase corresponds to the Li-poor region. In LMF93 with fewer $[\text{Fe}(\text{CN})_6]$ vacancies, the cooperative JT distortion due to Mn^{3+} causes the tetragonal distortion. More detailed discussions are described elsewhere [18].

3.2. Cobalt PBA. Figure 9 shows the OCV discharge curve of NCF90 film against Li measured at 0.8 C. The discharge curve shows plateau features. We tentatively divided the discharge curve into three plateaus, that is, plateaus I, II, and III. The observed capacity (=139 mAh/g) is comparable to the ideal value (=138 mAh/g).

Figure 10 shows the XRD patterns of powered LCF90 against x . All the reflections can be indexed with the face-centered cubic setting, as shown in parentheses. At $x = 1.2$, two-phase feature is observed. In addition, the reflections discontinuously shift to the lower angle side between $x = 1.0$ and 1.2. These indicate a first-order structural transition induced by Li^+ intercalation. The lattice constants (a) are refined by Rietveld analysis with the face-centered cubic ($\text{Fm}\bar{3}\text{m}; Z = 4$) model.

Figure 11(a) shows the XAS spectra of LCF90 films around the Co K-edge against x . The XAS spectrum at $x = 0.0$ coincides with that of LS Co^{3+} , while the spectrum at 1.6 coincides with that of HS Co^{2+} [30]. The electronic

configuration at $x = 0.00$ becomes $\text{Co}^{3+}-\text{Fe}^{2.78+}$ if we assume the charge neutrality: $\text{Li}_{1.6}\text{Co}^{\text{II}}[\text{Fe}^{\text{II}}(\text{CN})_6]_{0.90} \rightarrow 1.6\text{Li}^+ + \text{Co}^{\text{III}}[\text{Fe}^{\text{II}}_{0.33}\text{Fe}^{\text{III}}_{0.67}(\text{CN})_6]_{0.90}$. In the intermediate x -region, the average Co valences are determined by the spectral decomposition as follows. The XAS spectra $[\phi(x)]$ at x are decomposed into $\phi(0.0)$ and $\phi(1.6)$ as $\phi(x) = \chi\phi(0.0) + (1 - \chi)\phi(1.6)$, where χ is an adjustable parameter. The average Co valence is expressed as $\chi + 2$. Note that $\phi(0.6)$ [$\phi(1.4)$] is essentially identical to $\phi(0.0)$ [$\phi(1.6)$]. In other words, Co is divalent in $0.0 < x < 0.6$ while it is trivalent in $1.4 < x < 1.6$. Figure 4(b) shows the XAS spectra of LCF90 films around the Fe K-edge against x . The peak energy at $x = 1.6$ coincides with that of LS Fe^{2+} [30]. The blue-shift with decrease in x indicates partial formation of LS Fe^{3+} . The average Fe valence (V_{Fe}) is determined by the peak energy (E) as $V_{\text{Fe}} = -6569.0 + 0.92204E$. It is, however, difficult to extract any effective information on the Fe valence due to the big error bars.

Thus obtained lattice constant (a), Co valence, and the Fe valence are plotted in Figure 12. The Co valence remains trivalent in plateau I ($0.0 < x < 0.7$), while it remains divalent in plateau III ($1.1 < x < 1.6$). On the other hand, the Co valence steeply decreases with x in plateau II ($0.7 < x < 1.1$). These observations suggest that the plateaus I, II, and III are ascribed to the reduction processes of Fe^{3+} , Co^{3+} , and Fe^{3+} , respectively. Around the boundary between plateaus II and III, a first-order structural phase transition takes place and the lattice constant discontinuously increases from 10.0 Å to 10.2 Å.

The most probable scenario for the structural phase transition is a cooperative charge-transfer from Fe^{2+} to Co^{3+} or the variation of the electronic configuration from $\text{Fe}^{2+} - \text{Co}^{2+\delta}$ to $\text{Fe}^{2+\delta} - \text{Co}^{3+}$. Actually, $\text{Na}_x\text{Co}[\text{Fe}(\text{CN})_6]_{0.71} \cdot 3.8\text{H}_2\text{O}$

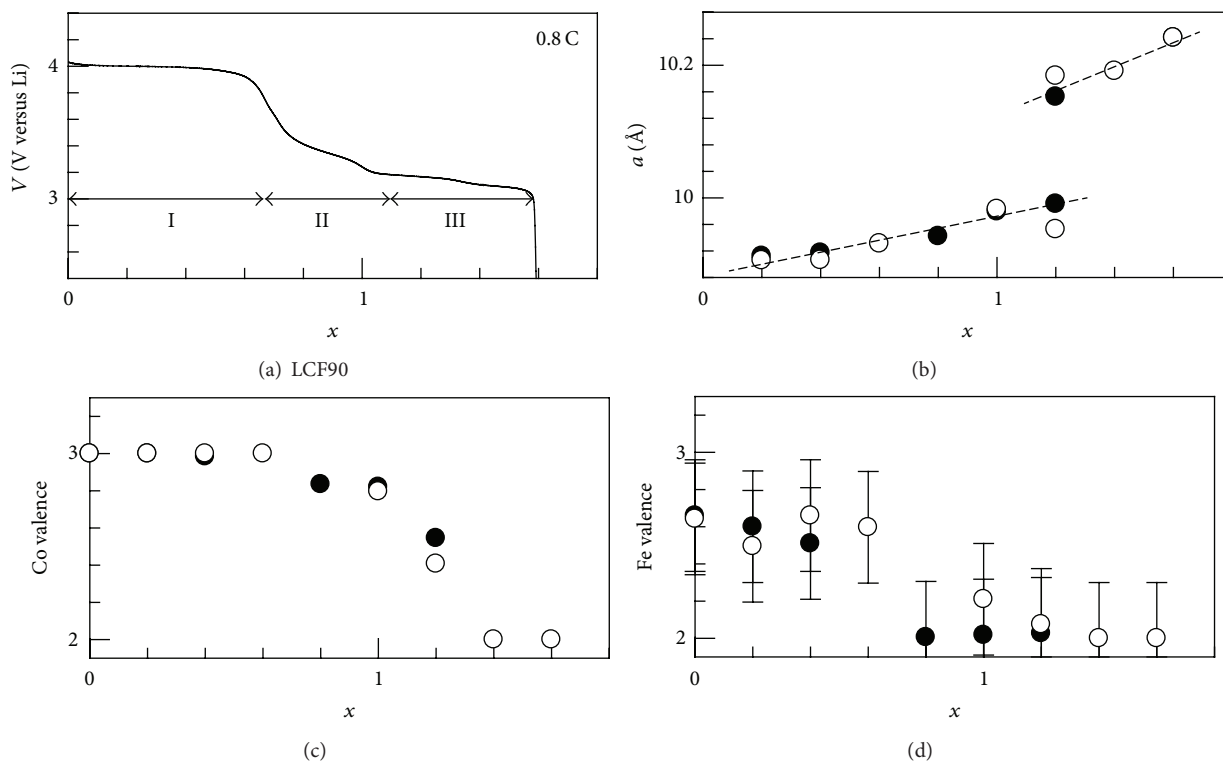


FIGURE 12: (a) Discharge curve, (b) lattice constant a , (c) Co valence, and (d) Fe valence of NCF90 against x . Open (filled) marks in (b), (c), and (d) mean that the data are obtained in the charge (discharge) run (cited from [20]).

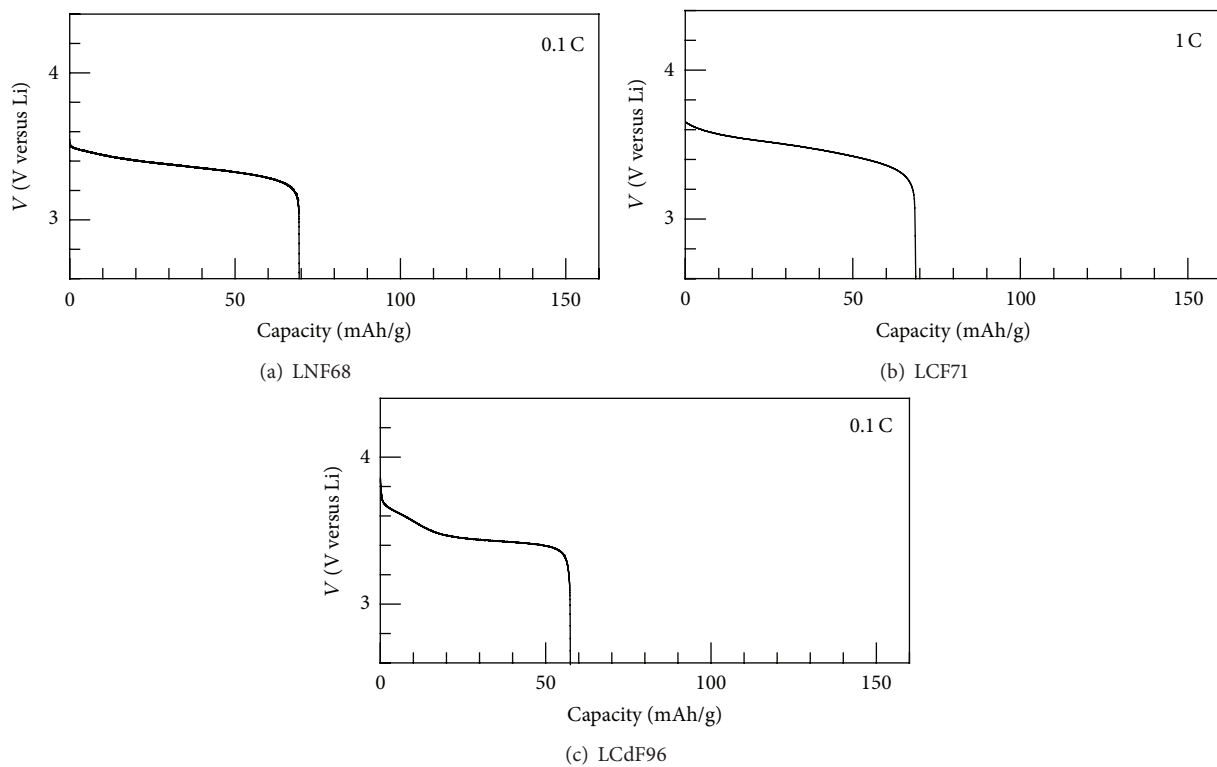


FIGURE 13: OCV discharge curves of (a) LNF68, (b) LCF71, and (c) LCdF96 films against Li (cited from [21]).

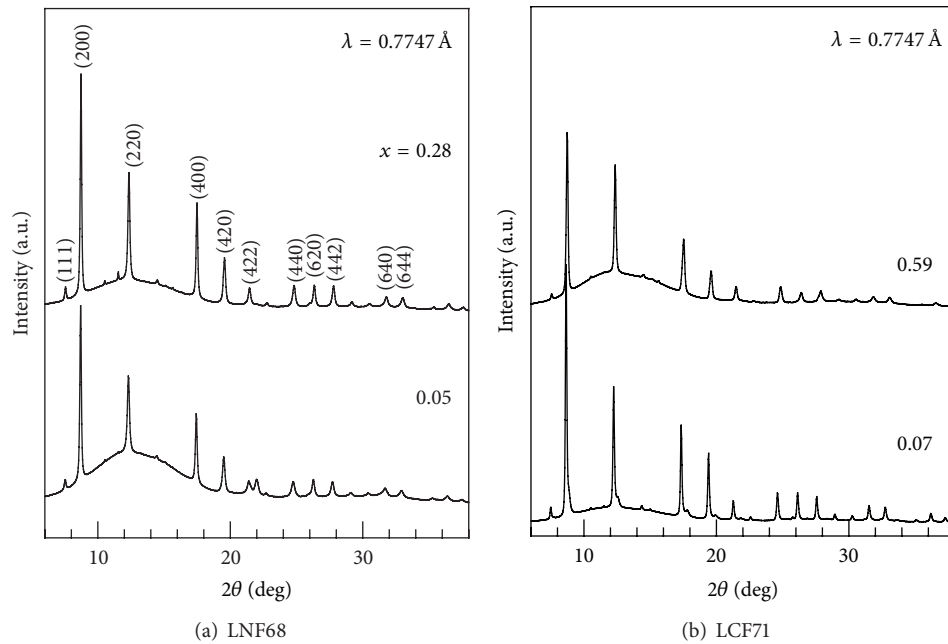


FIGURE 14: XRD pattern of powdered (a) LNF68 and (b) LCF71 against x . Values in parentheses represent indexes in the face-centered cubic setting (cited from [21]).

[33] exhibits a thermally induced structural phase transition due to the cooperative charge-transfer. This scenario well explains the abrupt reduction of the Co valence from 2.5 at $x = 1.2$ to 2.0 at 1.4. According to the scenario, the discontinuous increase in the lattice constant is ascribed to the bigger ionic radius ($=0.75 \text{ \AA}$) of HS Co^{2+} than that ($=0.55 \text{ \AA}$) of LS Co^{3+} . More detailed discussions are described elsewhere [20].

3.3. Other PBAs. Figure 13 shows the OCV discharge curves of PBA films against Li: (a) LNF68, (b) LCF71, and (c) LCdF96. The observed capacities, 69 mAh/g for LNF68, 70 mAh/g for LCF71, and 58 mAh/g for LCdF96, are comparable to the ideal values, 64 mAh/g for LNF68, 72 mAh/g for LCF71, and 64 mAh/g for LCdF96. The ideal values are calculated with assuming that only Fe takes part in the redox process.

Figure 14 shows the XRD patterns of powdered (a) LNF68 and (b) LCF71 against x . All the reflections can be indexed with the face-centered cubic setting, as shown in parentheses. The lattice constants (a) are refined by Rietveld analysis with the face-centered cubic ($\text{Fm}\bar{3}\text{m}$; $Z = 4$) model. Unfortunately, the powdered LCdF96 films are seriously unstable in air, and many impurity reflections are observed in the XRD pattern.

Figures 15(a) and 15(b) shows the XAS spectra of LNF68 films. The Fe K-edge spectrum exhibits red-shift with increase in x while the Ni K-edge spectra are essentially unchanged. This indicates that the reduction site is Fe in LNF68. Figures 15(c) and 15(d) show the XAS spectra of LCF71 films. Similarly to the case of LNF68, the Fe K-edge spectrum exhibits red-shift with increase in x while the Co K-edge spectra are essentially unchanged. This indicates that the reduction site is Fe in LCF71. Figures 15(e) and 15(f) show the

XAS spectra of LCdF96 films. Similarly to the case of LNF68, the Fe K-edge spectrum exhibits red-shift with increase in x while the Cd L_1 -edge spectra are essentially unchanged. This indicates that the reduction site is Fe in LCdF96.

4. Na^+ Intercalation

4.1. Manganese PBA. Figure 16 shows the OCV discharge curve of NMF83 film against Na measured at 0.6 C. The discharge curve shows two plateaus at 3.6 (plateau I) and 3.3 V (plateau II). The discharge voltages are slightly ($\sim 0.2\text{V}$) lower than those of LMF83. This is because the redox voltage ($= -3.71\text{V}$ versus SHE) of Na/Na^+ is higher than that ($= -3.04\text{V}$ versus SHE) of Li/Li^+ . The observed capacity ($= 130\text{ mAh/g}$) is comparable to the ideal value ($= 103\text{ mAh/g}$). The overall feature of the OCV discharge curve resembles that of LMF83 even though the curve is rather blurred in NMF83. This suggests that the plateaus I and II can be ascribed to the reduction processes of Mn^{3+} and Fe^{3+} , respectively. This assignments are confirmed by the IR spectroscopy around the CN stretching mode region [34].

Figure 17 shows the XRD patterns of powdered NMF83 against Na concentration (x). All the reflections can be indexed with the face-centered cubic setting, as shown in parentheses. No structural phase transition nor phase separation is observed in the entire x -region. The lattice constants (a) are refined by Rietveld analysis with the face-centered cubic ($\text{Fm}\bar{3}\text{m}$; $Z = 4$) model.

Thus obtained lattice constant (a) is plotted in Figure 18. In the plateau I, the lattice constant steeply increases from 10.40 \AA at $x = 0.00$ to $\sim 10.58 \text{ \AA}$ at $x \sim 0.3$. The expansion is ascribed to the bigger ionic radius ($= 0.83 \text{ \AA}$) of HS Mn^{2+}

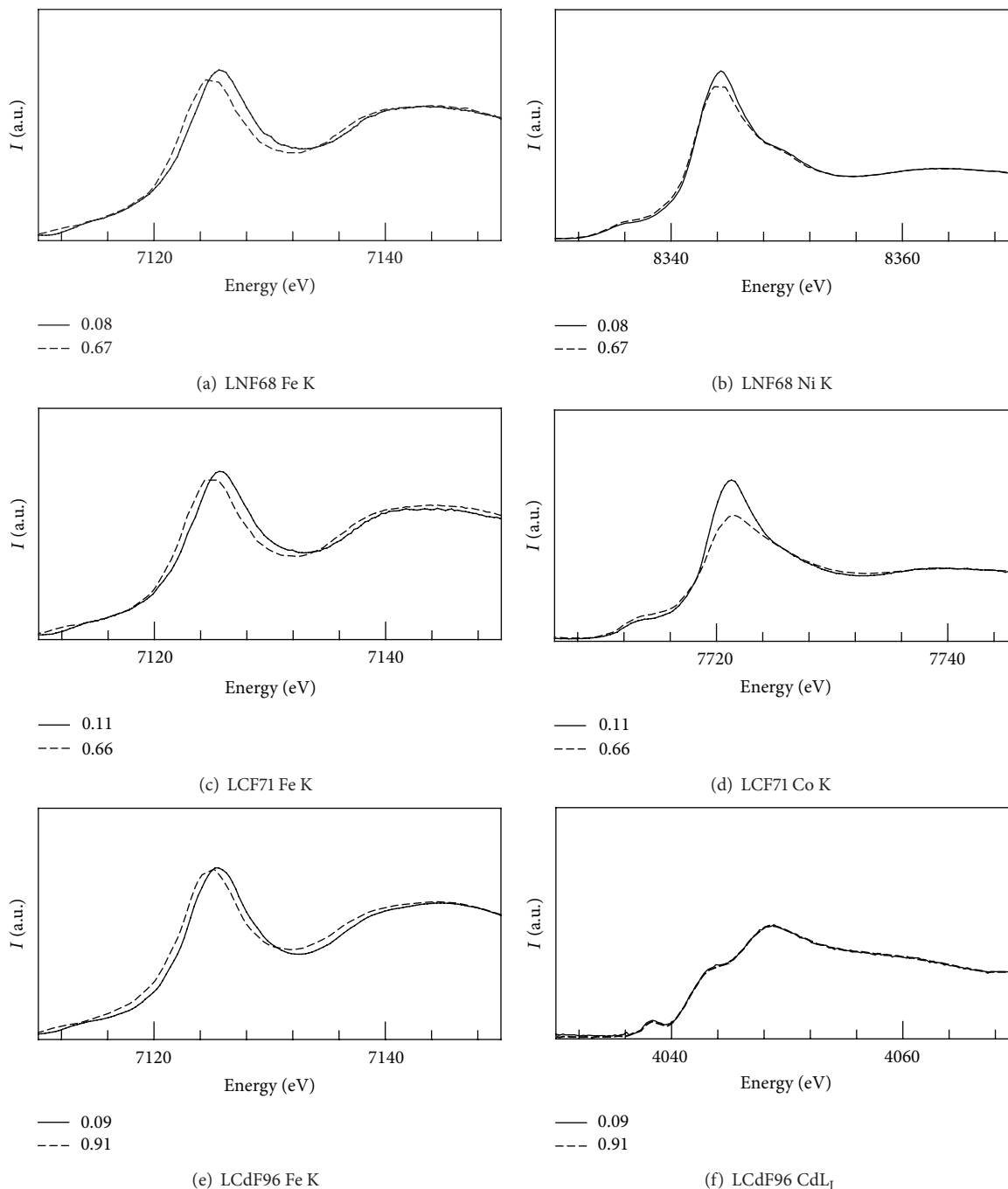


FIGURE 15: XAS spectra of LNF68 films against x around the (a) Fe K- and (b) Ni K-edges. XAS spectra of LCF71 films against x around the (c) Fe K- and (d) Co K-edges. XAS spectra of LCdF96 films against x around the (e) Fe K- and (f) Cd L_1 -edges (cited from [21]).

than that ($\approx 0.65 \text{ \AA}$) of HS Mn^{3+} . On the other hand, the lattice constant remains nearly constant in the plateau II. The overall feature of structural response of the host framework against Na^+ intercalation is nearly the same as that against Li^+ intercalation (see Figure 18(c)). This suggests that the guest-host interaction is rather weak in the PBA system, and the structural response of the host framework is governed by the ionic radius of the constituent M .

4.2. Cobalt PBA. Figure 19 shows the OCV discharge curve of NCF90 film against Na measured at 0.6 C. The discharge curve shows two plateaus at 3.8 (plateau I) and 3.4 V (plateau II). The discharge voltage in plateau I is slightly ($\sim 0.2 \text{ V}$) lower than that of LMF83. This is because the redox voltage of Na/Na^+ is higher than that of Li/Li^+ . The observed capacity ($\approx 133 \text{ mAh/g}$) is comparable to the ideal value ($\approx 127 \text{ mAh/g}$). The IR spectroscopy around the CN stretching mode and

TABLE 4: Experimental and calculated capacities of PBA films together with the structural responses.

Film	Capacity exp.	Capacity calc.	Ref.	Structural response
LMF83	115 mAh/g	110 mAh/g	[16]	Robust
LMF87	130 mAh/g	134 mAh/g	[16]	Phase separation
LMF93	143 mAh/g	153 mAh/g	[16]	Phase separation
LCF90	139 mAh/g	138 mAh/g	[22]	Phase transition
LCF71	70 mAh/g	72 mAh/g	[13]	Robust
LNF68	69 mAh/g	64 mAh/g	[13]	Robust
LCdF96	58 mAh/g	64 mAh/g	[13]	Robust
NMF83	130 mAh/g	103 mAh/g	[24]	Robust
NCF90	133 mAh/g	127 mAh/g	[25]	Robust

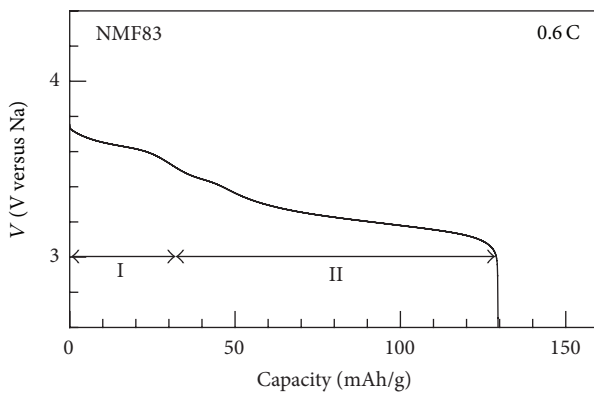
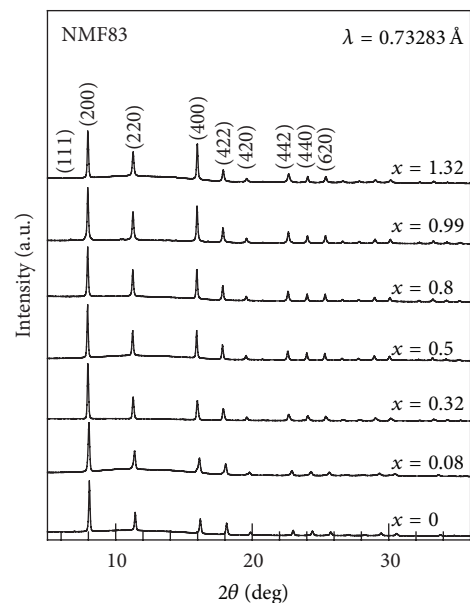


FIGURE 16: OCV discharge curves of NMF83 film against Na measured at 0.6 C. For convenience of explanation, we define plateaus I and II (cited from [14]).

XAS around the Fe K- and Co K-edges reveal that the plateaus I and II are ascribed to the reduction processes of Fe^{3+} and Co^{3+} , respectively [34].

Figure 20 shows the XRD patterns of powered NCF90 against x . All the reflections can be indexed with the face-centered cubic setting, as shown in parentheses. No structural phase transition nor phase separation is observed in the entire x -region, making a sharp contrast with LCF90 (Figure 21(c)). The lattice constants (a) are refined by Rietveld analysis with the face-centered cubic (Fm $\bar{3}$ m: $Z = 4$) model.

Thus obtained lattice constant (a) is plotted in Figure 21. In plateau I, the lattice constant remains nearly constant. In plateau II, a gradually increases from 9.96 Å at $x \sim 0.6$ to ~ 10.16 Å at $x \sim 1.6$. The expansion is ascribed to the bigger ionic radius ($=0.75$ Å) of HS Co^{2+} than that ($=0.45$ Å) of LS Co^{3+} . NCF90 exhibits no structural phase transition nor phase separation, which is advantageous for the stability and lifetime of the batteries. The disappearance of the structural phase transition in NCF90 is perhaps because the lattice constants of NCF90 in low- x -region are slightly (~ 0.02 Å) bigger than those of LCF90.

FIGURE 17: XRD pattern of powered NMF83 against Na concentration (x). Values in parentheses represent indexes in the face-centered cubic setting (cited from [14]).

5. Characteristics of PBA

5.1. Robust Framework against Li^+/Na^+ Intercalation. In conventional cathode materials, Li^+ deintercalation causes the structural phase separation and/or phase separation. For example, the Li deintercalation in LiCoO_2 causes the successive structural phase transitions and eventually produces CoO_2 with CdI_2 structure. In LiMn_2O_4 , $\gamma\text{-MnO}_2$ is produced at low Li concentration region. In LiFePO_4 , the Li deintercalation causes the phase separation into LiFePO_4 and FePO_4 .

In Table 4, we summarise the experimental and calculated capacities of PBA films together with the structural responses. Except for LMF87, LMF93, and LCF90, the host framework exhibits no structural phase transition nor phase separation in the entire x -region. In other words, they are robust against Li^+ and Na^+ intercalation. Surprisingly, in LMF83, LMF87, LMF93, LCF90, NMF83, and NCF90, the framework is stable

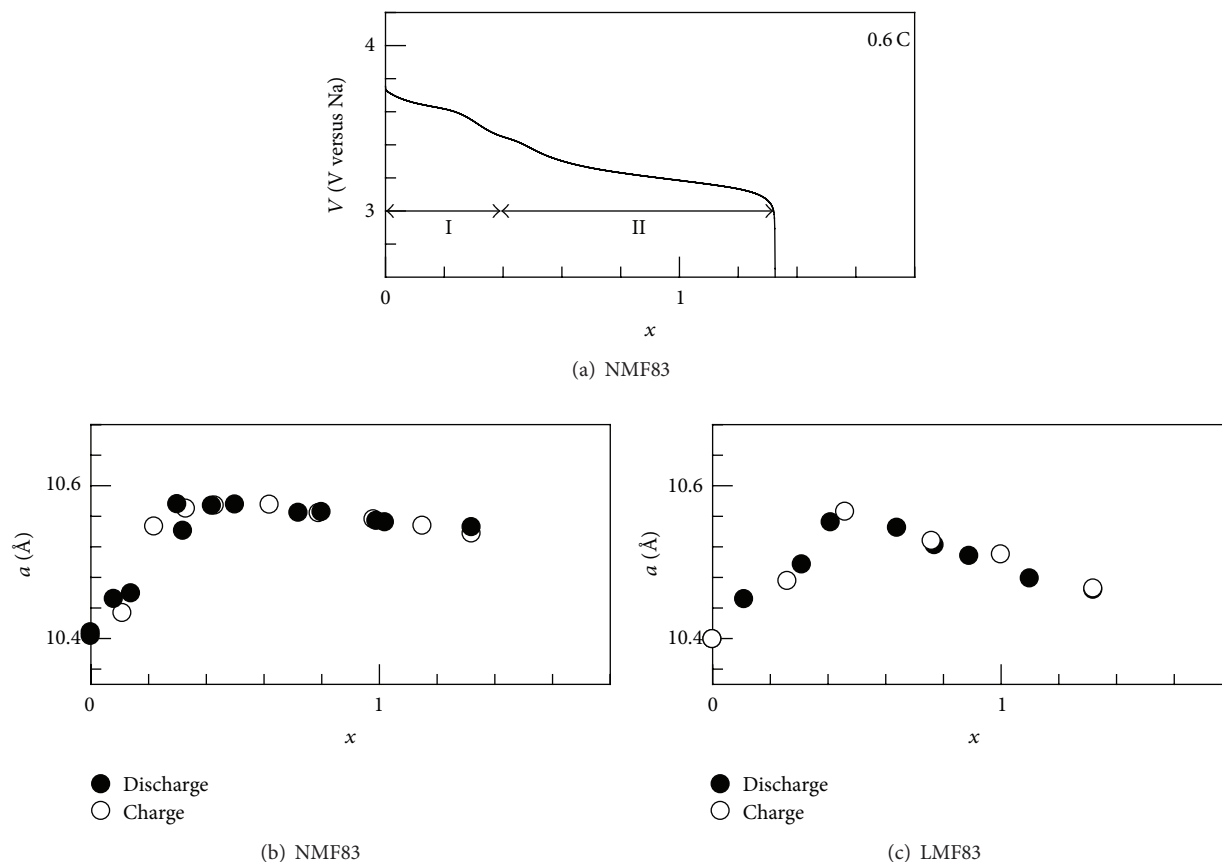


FIGURE 18: (a) Discharge curve, (b) lattice constant (a) of NMF83, and (c) lattice constant (a) of LMF83 against x . Open (filled) marks in (b), and (c) mean that the data are obtained in the charge (discharge) run (cited from [14]).

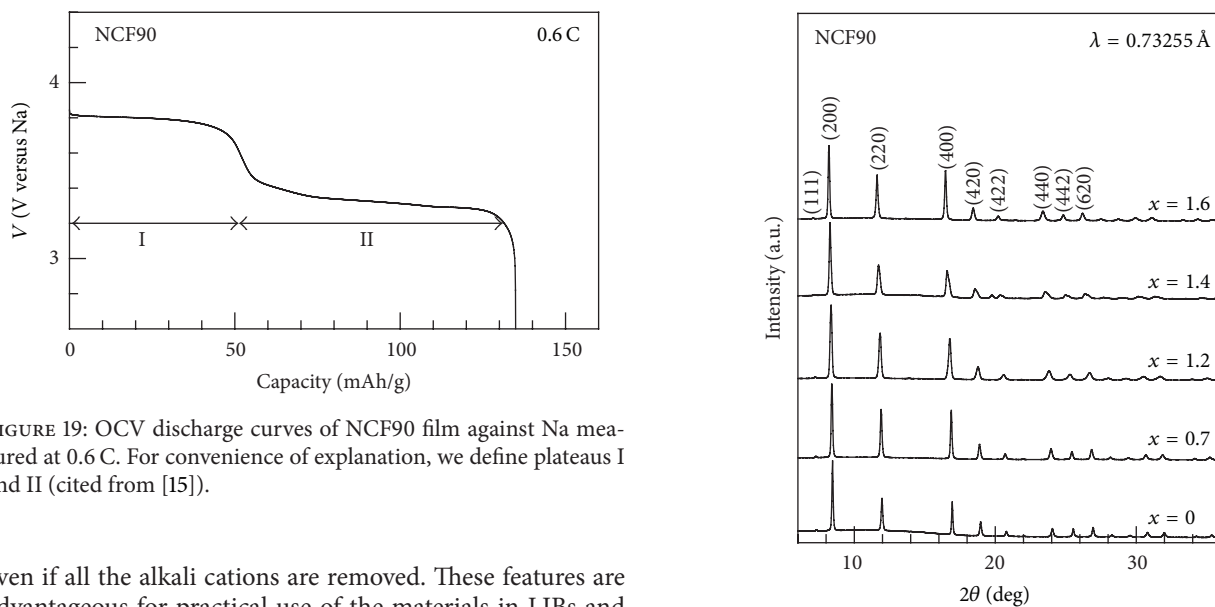


FIGURE 19: OCV discharge curves of NCF90 film against Na measured at 0.6 C. For convenience of explanation, we define plateaus I and II (cited from [15]).

even if all the alkali cations are removed. These features are advantageous for practical use of the materials in LIBs and SIBs. The robust nature of the host framework of the PBA system is probably ascribed to (1) the rigid 3D network and (2) the strong covalent nature of $M\text{-NC-Fe}$ bonding.

FIGURE 20: XRD pattern of powered NCF90 against Na concentration (x). Values in parentheses represent indexes in the face-centered cubic setting (cited from [15]).

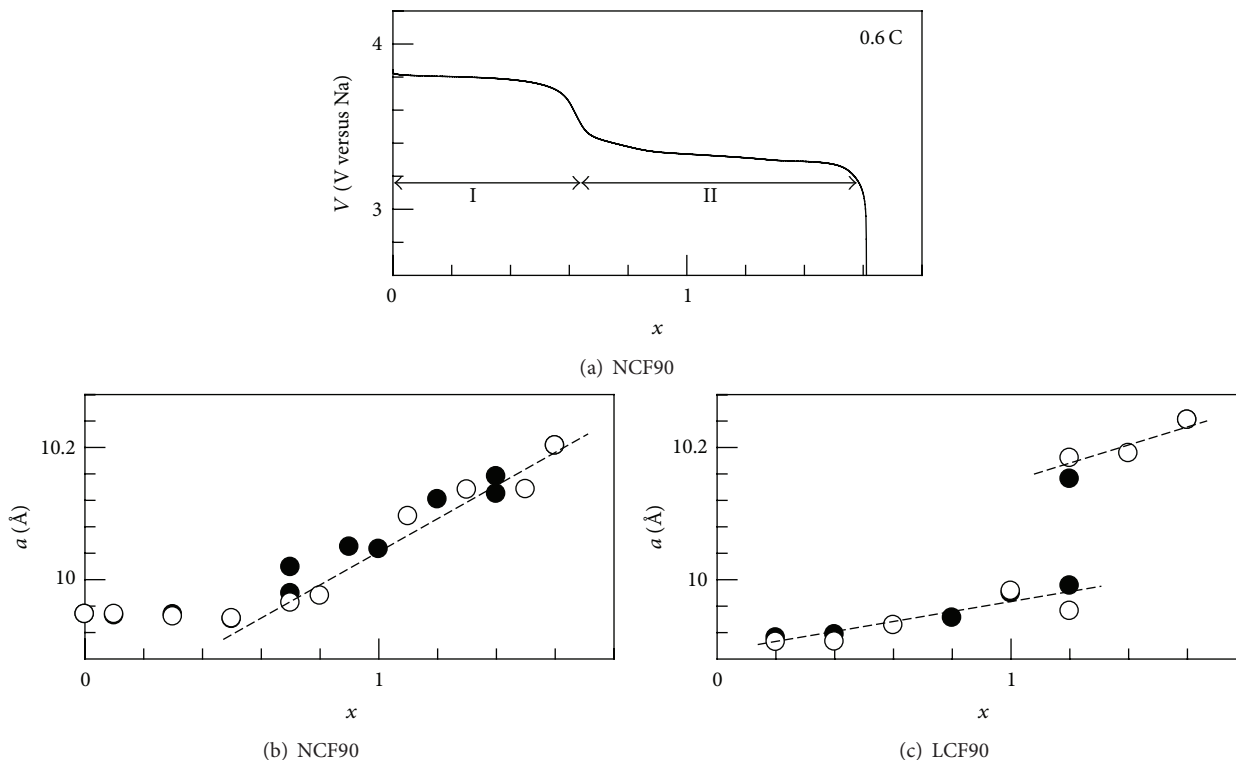


FIGURE 21: (a) Discharge curve, (b) lattice constant (a) of NCF90, and (c) a of LCF90 against x . Open (filled) marks in (b), and (c) mean that the data are obtained in the charge (discharge) run (cited from [15]).

5.2. Flat Plateau without Phase Separation. In conventional cathode materials, the plateau structure is ascribed to the phase separation. In other words, the voltage is pinned at the voltage of the decreasing phase, whose composition is unchanged against the charge/discharge process. For example, in LiFePO_4 , the Li^+ deintercalation causes phase separation into LiFePO_4 and FePO_4 [32]. The flat working voltage of 3.5 V is determined by LiFePO_4 .

The OCV discharge curves of PBA films exhibit flat plateaus, for example, the 3.8 and 3.5 V plateaus in LMF83 and the 3.8 and 3.4 V plateaus in NCF90. Importantly, our spectroscopic investigation reveals that these flat plateaus cannot be ascribed to the phase separation. The flat plateaus, which are advantageous for the practical use of the materials in LIBs and SIBs, are intrinsic nature of the host framework. The flat plateaus are reasonably ascribed to the weak interaction (J) between the guest Li^+/Na^+ . The weak-J is originated in (1) the longer inter-ion distance (~ 5 Å) as well as (2) the separation of the ions by the square window of the framework.

6. Summary

The SR XRD and XAS reveal the following characteristic features of PBA against Li^+/Na^+ intercalation/deintercalation.

- (1) Host framework is robust against Li^+/Na^+ intercalation/deintercalation.
- (2) Discharge curve exhibits intrinsic flat plateaus, which cannot be ascribed to the phase separation.

The robust nature of the host framework is probably ascribed to (1) the rigid 3D network and (2) the strong covalent nature of $M\text{-NC-Fe}$ bonding. The intrinsic flat plateaus are reasonably ascribed to the weak-J between the guest Li^+/Na^+ . The weak-J is originated in (1) the longer inter-ion distance (~ 5 Å) as well as (2) the separation of the ions by the square window of the framework.

Acknowledgments

This work was supported by the Canon Foundation, Mitsubishi Foundation, and also by a Grant-in-Aid for Scientific Research (nos. 25620036 and 23249) from the Ministry of Education, Culture, Sports, Science and Technology, Japan. The SR XRD experiments were performed at the BL02B2 beamline of SPring-8 with the approval of the Japan Synchrotron Radiation Research Institute (Proposal nos. 2012A1094, 2011B1066, 2011A1048, and 2010B1063). The SR XRD and XAS experiments were performed under the approval of the Photon Factory Program Advisory Committee (Proposal nos. 2010G502, 2011G501, 2013G001, and 2013G068). The elementary analysis of the films was performed at the Chemical Analysis Division, Research Facility Center for Science and Engineering, University of Tsukuba.

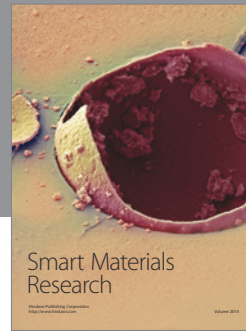
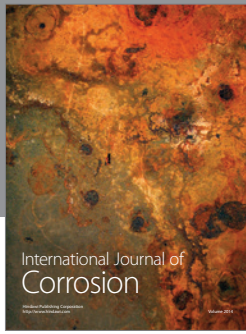
References

- [1] M. Armand and J.-M. Tarascon, "Building better batteries," *Nature*, vol. 451, no. 7179, pp. 652–657, 2008.

- [2] J. B. Goodenough and Y. Kim, "Challenges for rechargeable Li batteries," *Chemistry of Materials*, vol. 22, no. 3, pp. 587–603, 2010.
- [3] S. W. Kim, D. H. Seo, X. Ma, G. Ceder, and K. Kang, "Electrode materials for rechargeable sodium ion batteries: potential alternatives to current lithium ion batteries," *Advanced Energy Materials*, vol. 2, no. 7, pp. 710–721, 2012.
- [4] S. P. Ong, V. L. Chevrier, G. Hautier et al., "Voltage, stability and diffusion barrier differences between sodium-ion and lithium-ion intercalation materials," *Energy and Environmental Science*, vol. 4, no. 9, pp. 3680–3688, 2011.
- [5] S. Komaba, C. Takei, T. Nakayama, A. Ogata, and N. Yabuuchi, "Electrochemical intercalation activity of layered NaCrO_2 vs. LiCrO_2 ," *Electrochemistry Communications*, vol. 12, no. 3, pp. 355–358, 2010.
- [6] A. Caballero, L. Hernán, J. Morales, L. Sánchez, J. Santos Peña, and M. A. G. Aranda, "Synthesis and characterization of high-temperature hexagonal $\text{P}_2\text{-Na}_{0.6}\text{MnO}_2$ and its electrochemical behaviour as cathode in sodium cells," *Journal of Materials Chemistry*, vol. 12, no. 4, pp. 1142–1147, 2002.
- [7] S. Komaba, W. Murata, T. Ishikawa et al., "Electrochemical Na insertion and solid electrolyte interphase for hard-carbon electrodes and application to Na-ion batteries," *Advanced Functional Materials*, vol. 21, no. 20, pp. 3859–3867, 2011.
- [8] T. Matsuda, J. E. Kim, K. Ohoyama, and Y. Moritomo, "Universal thermal response of the Prussian blue lattice," *Physical Review B*, vol. 79, no. 17, Article ID 172302, 4 pages, 2009.
- [9] N. Imanishi, T. Morikawa, J. Kondo et al., "Lithium intercalation behavior into iron cyanide complex as positive electrode of lithium secondary battery," *Journal of Power Sources*, vol. 79, no. 2, pp. 215–219, 1999.
- [10] N. Imanishi, T. Morikawa, J. Kondo et al., "Lithium intercalation behavior of iron cyanometallates," *Journal of Power Sources*, vol. 81–82, pp. 530–534, 1999.
- [11] M. Okubo, D. Asakura, Y. Mizuno et al., "Switching redox-active sites by valence tautomerism in prussian blue analogues $\text{A}_x\text{Mn}_y[\text{Fe}(\text{CN})_6] \cdot n\text{H}_2\text{O}$ (A = K, Rb): Robust frameworks for reversible Li storage," *Journal of Physical Chemistry Letters*, vol. 1, no. 14, pp. 2063–2071, 2010.
- [12] T. Matsuda and Y. Moritomo, "Thin film electrode of Prussian blue analogue for Li-ion battery," *Applied Physics Express*, vol. 4, no. 4, Article ID 047101, 3 pages, 2011.
- [13] Y. Lu, L. Wang, J. Cheng, and J. B. Goodenough, "Prussian blue: a new framework of electrode materials for sodium batteries," *Chemical Communications*, vol. 48, pp. 6544–6546, 2012.
- [14] T. Matsuda, M. Takachi, and Y. Moritomo, "A sodium manganese ferrocyanide thin film for Na-ion batteries," *Chemical Communications*, vol. 49, no. 27, pp. 2750–2752, 2013.
- [15] M. Takachi, T. Matsuda, and Y. Moritomo, "Cobalt hexacyanoferrate as cathode material for Na^+ secondary battery," *Applied Physics Express*, vol. 6, no. 2, Article ID 0258028, 3 pages, 2013.
- [16] A. Gotoh, H. Uchida, M. Ishizaki et al., "Simple synthesis of three primary colour nanoparticle inks of Prussian blue and its analogues," *Nanotechnology*, vol. 18, no. 34, Article ID 345609, 2007.
- [17] S. Hara, H. Tanaka, T. Kawamoto et al., "Electrochromic thin film of Prussian blue nanoparticles fabricated using wet process," *Japanese Journal of Applied Physics II*, vol. 46, no. 36–40, pp. L945–L947, 2007.
- [18] Y. Kurihara, T. Matsuda, and Y. Moritomo, "Structural properties of manganese hexacyanoferrates against Li concentration," *Japanese Journal of Applied Physics*, vol. 52, no. 17, Article ID 017301, 7 pages, 2012.
- [19] T. Matsuda and Y. Moritomo, "Two-electron reaction without structural phase transition in nanoporous cathode materials," *Journal of Nanotechnology*, vol. 2012, Article ID 5698148, 8 pages, 2012.
- [20] M. Takachi, T. Matsuda, and Y. Moritomo, "Structural, electronic, and electrochemical properties of $\text{Li}_x\text{Co}[\text{Fe}(\text{CN})_6]_{0.90} \cdot 2.9\text{H}_2\text{O}$," *Japanese Journal of Applied Physics*, vol. 52, no. 4, Article ID 044301, 7 pages, 2013.
- [21] Y. Moritomo, M. Takachi, Y. Kurihara, and T. Matsuda, "Thin film electrodes of Prussian blue analogues with rapid Li^+ intercalation," *Applied Physics Express*, vol. 5, no. 4, Article ID 41801, 3 pages, 2012.
- [22] N. Bagkar, C. A. Betty, P. A. Hassan, K. Kahali, J. R. Bellare, and J. V. Yakhmi, "Self-assembled films of nickel hexacyanoferrate: electrochemical properties and application in potassium ion sensing," *Thin Solid Films*, vol. 497, no. 1–2, pp. 259–266, 2006.
- [23] W. Jin, A. Toutianoush, M. Pyrasch et al., "Self-assembled films of Prussian blue and analogues: structure and morphology, elemental composition, film growth, and nanosieving of ions," *Journal of Physical Chemistry B*, vol. 107, no. 44, pp. 12062–12070, 2003.
- [24] M. Pyrasch, A. Toutianoush, W. Jin, J. Schnepf, and B. Tieke, "Self-assembled films of Prussian Blue and analogues: optical and electrochemical properties and application as ion-sieving membranes," *Chemistry of Materials*, vol. 15, no. 1, pp. 245–254, 2003.
- [25] Y. Moritomo, K. Igarashi, J. Kim, and H. Tanaka, "Size dependent cation channel in nanoporous prussian blue lattice," *Applied Physics Express*, vol. 2, no. 8, Article ID 085001, 3 pages, 2009.
- [26] Y. Moritomo, Y. Kurihara, T. Matsuda, and J. Kim, "Structural phase diagram of Mn-Fe cyanide against cation concentration," *Journal of the Physical Society of Japan*, vol. 80, no. 10, Article ID 103601, 4 pages, 2011.
- [27] E. Nishibori, M. Takata, K. Kato et al., "The large Debye-Scherrer camera installed at SPring-8 BL02B2 for charge density studies," *Nuclear Instruments and Methods in Physics Research A*, vol. 467–468, no. 2, pp. 1045–1048, 2001.
- [28] F. Izumi and K. Momma, "Three-dimensional visualization in powder diffraction," *Diffusion and Defect Data B*, vol. 130, pp. 15–20, 2007.
- [29] B. Ravel and M. Newville, "ATHENA, ARTEMIS, HEPHAESTUS: data analysis for X-ray absorption spectroscopy using IFEFFIT," *Journal of Synchrotron Radiation*, vol. 12, no. 4, pp. 537–541, 2005.
- [30] Y. Kurihara, H. Funashima, M. Ishida et al., "Electronic structure of hole-doped transition metal cyanides," *Journal of the Physical Society of Japan*, vol. 79, no. 4, Article ID 044710, 7 pages, 2010.
- [31] K. Kato, Y. Moritomo, M. Takata et al., "Direct observation of charge transfer in double-perovskite-like $\text{RbMn}[\text{Fe}(\text{CN})_6]$," *Physical Review Letters*, vol. 91, no. 25, Article ID 255502, 4 pages, 2003.
- [32] A. K. Padhi, K. S. Nanjundaswamy, and J. B. Goodenough, "Phospho-olivines as positive-electrode materials for rechargeable lithium batteries," *Journal of the Electrochemical Society*, vol. 144, no. 4, pp. 1188–1194, 1997.
- [33] F. Nakada, H. Kamioka, Y. Moritomo, J. E. Kim, and M. Takata, "Electronic phase diagram of valence-controlled cyanide:

$\text{Na}_{0.84-\delta}\text{Co}[\text{Fe}(\text{CN})_6]_{0.71}\cdot 3.8\text{H}_2\text{O}$ ($0 < \delta < 0.61$),” *Physical Review B*, vol. 77, no. 22, Article ID 224436, 7 pages, 2008.

- [34] M. Takachi, T. Matsuda, and Y. Moritomo, “Redox reaction in Prussian blue analogue films with fast Na^+ intercalation,” *Japanese Journal of Applied Physics*, vol. 52, no. 9, Article ID 09020, 4 pages, 2013.



Hindawi

Submit your manuscripts at
<http://www.hindawi.com>

